# Assessment of InSAR tropospheric signal correction methods

Haji-Aghajany, Saeid; Amerian, Yazdan

**DOI**
10.1117/1.JRS.14.044503

**Publication date**
2020

**Document Version**
Final published version

**Published in**
Journal of Applied Remote Sensing

# Assessment of InSAR tropospheric signal correction methods

**Saeid Haji-Aghajany**[a,b] **and Yazdan Amerian**[a,*]

[a]K. N. Toosi University of Technology, Faculty of Geodesy and Geomatics Engineering, Tehran, Iran

[b]Delft University of Technology, Faculty of Civil Engineering and Geosciences, Delft, The Netherlands

**Abstract.** Tropospheric signals are considered as one of the most important performance limitations to compute the deformations caused by earthquake, subsidence, volcano, and so on using interferometric synthetic aperture radar (InSAR) technique. Various correction methods have been proposed to reduce the effect of these signals in displacement fields in previous research works. Different types of correction methods are used to estimate the tropospheric signal on InSAR observations. For this purpose, meteorological data derived from ERA-Interim (ERA-I) data, Weather Research and Forecasting (WRF) model, and Advanced Synthetic Aperture Radar/ENVISAT acquisitions are used. ERA-I reanalysis data and a locally run WRF model are also used to compute the tropospheric corrections with integral of the air refractivity method, which is called integration method. Also, the ability of ray tracing techniques to reduce the effect of the tropospheric signal in unwrapped interferogram is compared with integration method. To carry out a comprehensive study, the effects of correction methods are studied in two different areas. The results of the ray tracing methods have a significant difference with the results obtained from integration method and are more efficient when the weather condition between two satellite acquisitions is more different. The results show that the three-dimensional ray tracing method can reduce the root-mean-square error of the results up to 4.8 cm compared to the integration methods. © *2020 Society of Photo-Optical Instrumentation Engineers (SPIE)* [DOI: 10.1117/1.JRS.14.044503]

**Keywords:** tropospheric signal; interferometric synthetic aperture radar; ray tracing; ERA-Interim; Weather Research and Forecasting.

Paper 200281 received Apr. 15, 2020; accepted for publication Oct. 1, 2020; published online Oct. 14, 2020.

## 1 Introduction

Interferometric synthetic aperture radar (InSAR) is a powerful technique for topographic and ground surface deformation mapping over vast areas using radar acquisitions. Disregarding coherence loss, the main limitation of radar interferometry in measuring ground displacements is due to phase propagation delays caused by the atmosphere.[1] Atmospheric propagation delays are a geophysical signal affecting each pixel of the radar scene. Based on the previous research, these can potentially be modeled and corrected. These signals are the main limiting factor in the accuracy of the InSAR technique. In this technique, atmospheric signals are caused by effects of ionosphere and air refractivity variations in the troposphere. Generally, the effect of the ionospheric air refractivity on short-wavelength InSAR is negligible.[2] Air refractivity variations in troposphere layer are due to the spatiotemporal variations of relative humidity, temperature, and pressure. The temperature and pressure can be mostly considered vertically stratified, which lead to a large phase delay varying along elevation in a radar scene. On the contrary, the relative humidity varies both vertically and laterally over short distances.[3]

Numerous studies have been addressed the corrections of tropospheric delays empirically based on the correlation between the delay and the topographic elevation of areas far from

*Address all correspondence to Yazdan Amerian, amerian@kntu.ac.ir

1931-3195/2020/$28.00 © 2020 SPIE

the main deformation,[4–6] stacking independent InSAR data,[7,8] and characterizing the statistical properties of phase delay patterns.[9] These approaches are utilized to construct covariance matrices of observations and also to separate stochastic noise from ground motion signal.[9] Tropospheric delay estimation using external data is one of the most widely used methods for computing the required tropospheric corrections in InSAR displacement fields.[10] In previous studies, the tropospheric delay has been computed in zenith direction using integration method, and the incidence angle of the signal has been used to convert the computed tropospheric delay along zenith to the line-of-sight (LOS) direction.[10]

Ray tracing methods are the most precise techniques to reconstruct the real path of signal propagation using atmospheric parameters. Ray tracing techniques have many applications in various fields including geodesy and remote sensing.[11–17] In these methods, tropospheric delay is the difference between the straight geometrical path and real one excluded from ray tracing. Two-dimensional (2D) and three-dimensional (3D) methods have been proposed for ray tracing techniques by researchers. 2D methods were developed based on fixed azimuth angle for signal propagation, and in 3D method, there is no fixed azimuth angle criterion for signal propagation.[15]

A number of Advanced Synthetic Aperture Radar (ASAR)/ENVISAT acquisitions from two different locations in Iran are processed. Then, several interferograms with different weather conditions are selected to perform tropospheric correction. In this paper, the effect of the tropospheric corrections obtained by various ray tracing methods on InSAR displacement fields is investigated. The European Center for Medium-Range Weather Forecasts (ECMWF) ERA-Interim (ERA-I) data are used as initial values for computing tropospheric delay using different ray tracing methods. ERA-I reanalysis data and a locally run Weather Research and Forecasting (WRF) model also used to compute the tropospheric corrections with integration method. Finally, the interferograms are corrected using tropospheric delays computed from above-mentioned methods and results are compared. In the following, the basics of the InSAR and tropospheric correction methods is provided. Then, the study areas, data set and are presented. The obtained results from the different approaches, validation, and discussion are presented in the last section.

## 2 InSAR Technique

The InSAR technique can measure the projection of the deformation vector onto the LOS direction, defined as the shortest path from a given point on ground to the SAR antenna phase center. InSAR provides unique capabilities for the study of crustal deformation.[18] The basic InSAR data are called an interferogram, which represents the per-pixel phase difference between two SAR acquisitions. Recently developed InSAR processing approaches use data from multiple acquisitions to estimate displacement time series include persistent scatterer interferometry and small-baseline subset methods.[19,20] For a given interferogram, considering the effects of topography error, atmospheric path delay, orbital error, and other thermal noise errors, the observed InSAR phase change can be expressed as[1]

$$\Phi = \Phi_{def} + \Phi_{topo} + \Phi_{atm} + \Phi_{orbit} + \Phi_{noise}, \tag{1}$$

where $\Phi_{def}$ is the deformation phase along the LOS direction, $\Phi_{topo}$ is the phase resulted from the topography effect, $\Phi_{atm}$ is the phase resulted from the atmospheric delay, $\Phi_{orbit}$ is the phase due to orbital paths, and $\Phi_{noise}$ is the phase related to other thermal noise errors.[1] Since we decide to extract the displacement field from InSAR observations, namely, $\Phi_{def}$, the other contributions in the observable InSAR phase should be modeled from auxiliary data and removed from Eq. (1). In this study, for the reduction of the topography and orbital effects, the Advanced Spaceborne Thermal Emission and Reflection Radiometer (ASTER) digital elevation model (DEM) with resolution of 30 m and orbital files are used, respectively.

When the radar signals propagate through the inhomogeneous troposphere, which has a slightly higher index of refraction, they undergo a delay that produces a bias term in the observed LOS. Tropospheric effects are due to the temperature, relative humidity, and pressure variations between two acquisitions.[10] How to reduce this effect is one of the most important challenges in achieving high-precision InSAR displacement fields.

## 3 Tropospheric Correction Methods

As previously mentioned, one of the methods for reducing the effect of the troposphere on the InSAR displacement field is to compute the difference between the tropospheric delays in the two acquisition times and reduce it from the amount of obtained displacement field. In this section, the integration method and different methods of ray tracing technique are discussed for determining the tropospheric delay.

### 3.1 *Integration Method*

Interferometric radar analysis is done using commentary exact time delay and differential phase shifts. When the signals propagate through the troposphere, the velocity is lowered slightly and the observations contaminated due to spatially variable delays.[10] The zenith excess path ($l$) is computed from the integral between the surface elevation ($z_0$) and the atmosphere top (at $z \sim \infty$) of the air refractivity:[10]

$$l(z) = 10^{-6}\left\{\frac{k_1 R_d}{g_m}P(z_0) + \int_{z_0}^{z}\left[\left(k_2 - \frac{R_d}{R_v}k_1\right)\frac{e}{T} + k_3\frac{e}{T^2}\right]\mathrm{d}z\right\}, \tag{2}$$

$$k_1 = 0.776\ \mathrm{KPa}^{-1}, \quad k_2 = 0.716\ \mathrm{KPa}^{-1}, \quad k_3 = 3.75\times 10^3\ \mathrm{K}^2\mathrm{Pa}^{-1}, \tag{3}$$

where $R_d$ (287.05 J/kg/K) is the specific gas constant for dry air, $R_v$ (461.495 J/kg/K) is the specific gas constant for water vapor, $P(z_0)$ is the surface pressure, $e$ is the water vapor pressure, $g_m$ is the gravitational acceleration $g$ averaged over the troposphere, and $T$ is the temperature in K.[3,10] The LOS single path atmospheric delay, $\delta L^{s}_{\mathrm{LOS}}(z)$, neglecting refractive bending, varies with elevation for each acquisition date is[1,10]

$$\delta L^{s}_{\mathrm{LOS}}(z) = \frac{10^{-6}}{\cos(\theta)}\left\{\frac{k_1 R_{\mathrm{d}}}{g_{\mathrm{m}}}[P(z) - P(z_0)] + \int_{z_0}^{z}\left[\left(k_2 - \frac{R_{\mathrm{d}}}{R_{\mathrm{v}}}k_1\right)\frac{e}{T} + k_3\frac{e}{T^2}\right]\mathrm{d}z\right\}, \tag{4}$$

where $\theta$ is the incidence angle of the radar signal. In most previous studies, the incidence angle is considered to be a constant for an image. But it should be noted that the value of this index varies for different pixels of an image. This may have a significant effect on the computation of tropospheric delay in some areas and times. It should be noted that the required meteorological parameters are accessible using different data and methods.[21–24]

### 3.2 *Ray Tracing Technique*

Ray tracing technique is the most precise technique to reconstruct the real path of signal propagation using atmospheric parameters, which is widely used for determining tropospheric delay. Ray tracing techniques are classified into two categories, 2D and 3D methods. In 2D methods, ray tracing is performed in a fixed azimuth, whereas in 3D method, the path of a ray can be retrieved in 3D space.[15,16] In this section, the theory of different methods of ray tracing is reviewed.

#### 3.2.1 *2D ray tracing methods*

One of the 2D ray tracing methods, called Thayer approach, was developed based on the relation of the refractive.[15]

The piecewise-linear (PWL) is another 2D ray tracing method with high accuracy and high processing speed.[12,15] The refractive index at different levels are used to apply the Snell's law of refraction and to calculate the tropospheric delay. The recursive relations used to calculate the tropospheric delay.

The refined piecewise-linear (RPWL) is a 2D ray tracing method to refine the previous method. This method uses intermediate compression levels to increase the accuracy of radiation tracking.[15]

More details and how to implement these methods can be found in previuos studies.[15]

### 3.2.2 *3D ray tracing method*

Unlike the 2D ray tracing methods, in 3D ray tracing method, the ray paths are not limited to a fixed azimuth plane and can be retrieved in 3D space.[15,25] This is the very important advantage of 3D ray tracing method to compute the tropospheric delay. This method is based on the Eikonal equations. The Eikonal equation represents a differential of $n(\vec{r})$. The values of the refractive index, which is necessary in this method, is derived from ERA-I data.[3] More details about this method algorithm and its application in tropospheric delay computation and reconstruction of signal path in tropospheric sensing could be found in previous research.[15,16]

## 4 Numerical Results

In this section, the study area and used data are introduced. Then the obtained numerical results are presented. Finally, the presented results are evaluated and discussed.

### 4.1 *Study Area and Data Set*

Iran is a country with very different weather conditions. The enormous variations in weather conditions make tropospheric layer monitoring important in this country. In addition, Iran is a country full of geodynamic phenomena such as earthquake and subsidence. Therefore, the use of InSAR technique is very common to achieve high accuracy in the computation of land deformations to study and monitor these disasters. Bushehr area in southwest of Iran was selected for this study. This is one of the hot and humid regions of Iran and is suitable for the purpose of this study. To conduct a comprehensive study, Tabriz area in northwest of Iran was selected as the second case study. The weather conditions of Tabriz are quite different with Bushehr. Therefore, the subject of this study can be appealing for those who are investigating the geodynamic and troposphere of Iran and similar areas. The geographic location of the study areas and their topography can be seen in Fig. 1.

The difference in weather conditions between two areas is visible in the maps of temperature and relative humidity from ERA-I data on the first day of June 2006 (Figs. 2 and 3). The average temperature and water vapor density in the center of the areas in the months of 2006 are reviewed better, as shown in Fig. 4. According to these maps, the difference between the weather conditions of the two areas in the two parameters of temperature and humidity, which plays a fundamental role in this study, is well visible.

In this paper, 14 acquisitions from ASAR/ENVISAT descending track 49 over Tabriz area and eight acquisitions from ASAR/ENVISAT ascending track 457 over Bushehr area have been used to produce interferograms. The ASTER DEM and ENVISAT precise orbits products has been used to correct the topography and orbital effects, respectively. Temporal and perpendicular baseline for the ASAR/ENVISAT acquisitions can be seen in Fig. 5.

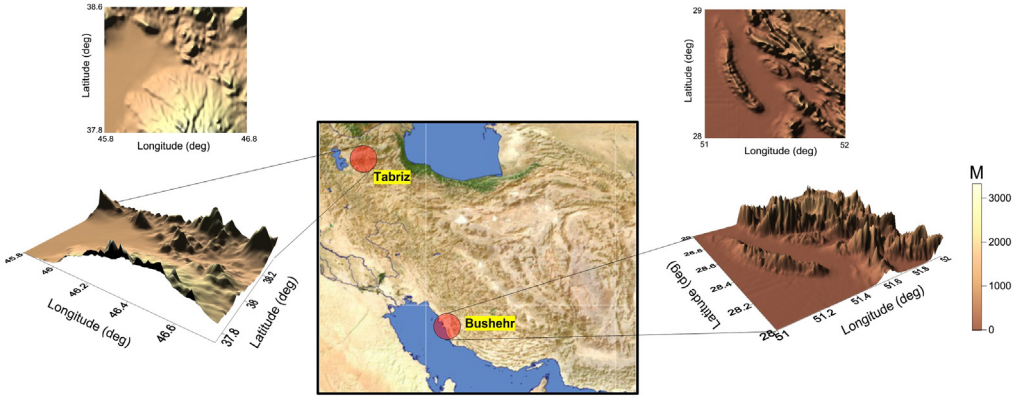


**Fig. 1** Study areas of this research and their DEM.

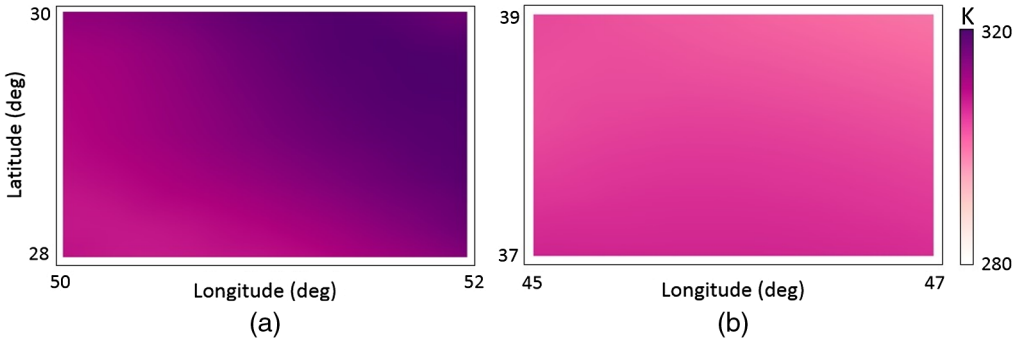


**Fig. 2** Sample of temperature map of two areas: (a) Bushehr and (b) Tabriz.

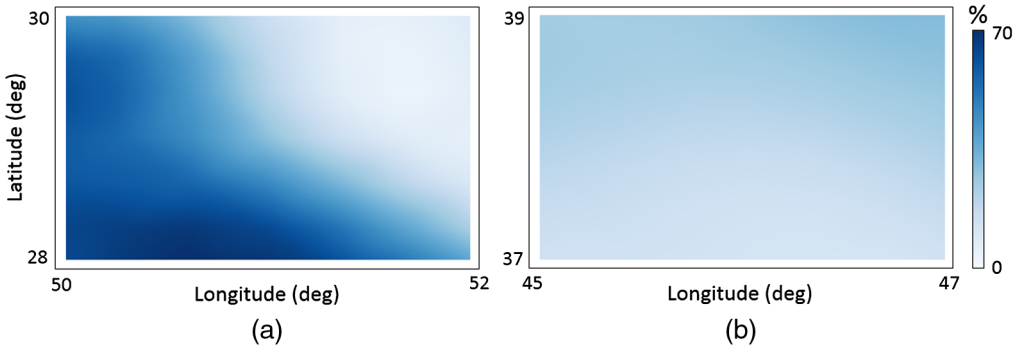


**Fig. 3** Sample of relative humidity map of two areas: (a) Bushehr and (b) Tabriz.

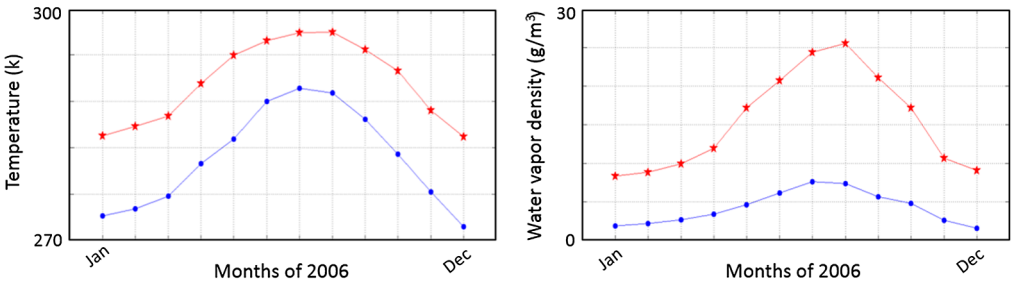


**Fig. 4** Average temperature and average water vapor density of the center of two areas in the months of 2006. (The red stars and blue circles are related to Bushehr and Tabriz areas, respectively).

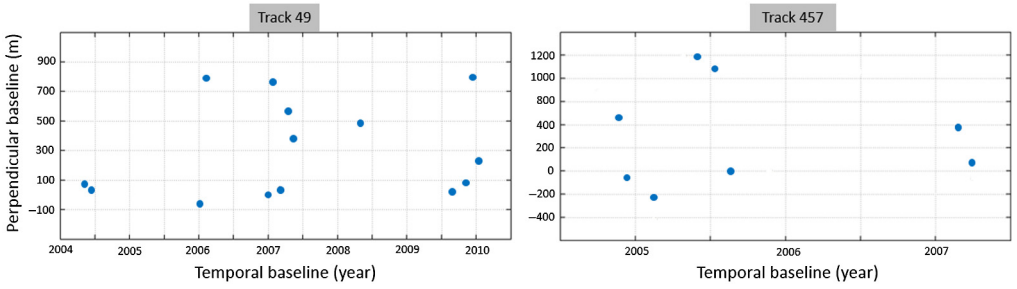


**Fig. 5** Baseline distribution through time for acquisitions.

The ERA-I data have been used to compute the tropospheric delay using integration method and to determine required values for ray tracing methods. This data provide values of several meteorological parameters on a global ~75 km day, at 0 am, 6 am, 12 pm, and 6 pm UT. The vertical stratification is described on 37 pressure levels, densely spaced at low elevation (interval of 25 hPa), with the highest level around 50 km (1 hPa).[21]

The Global Forecast System analysis (GFS) data have been used to run the WRF model and predict meteorological data. The GFS is a weather forecast model produced by the National Centers for Environmental Prediction (NCEP). Many of the atmospheric and land-soil variables are available through this dataset. The WRF model is a useful mesoscale numerical weather prediction system that is used for both atmospheric researches and operational weather forecasting. This model is equipped to a data assimilation system and a software with parallel processing system. The WRF model is used in a wide range of meteorological applications in different resolution from tens of meters to thousands of kilometers. The WRF model can produce simulations based on actual atmospheric conditions or idealized conditions. This model is currently in operational use at NCEP and other national meteorological centers and in real-time forecasting configurations at laboratories, universities, and companies.[26]

## 4.2 *WRF Model Configuration*

In this paper, The WRF model version 3.8 has been used with a parametrization set.[27] The WRF model runs with a set of parameterization schemes, including cloud microphysics, land surface processes, and atmospheric radiation. Output data from the WRF model can be used to generate the tropospheric delay at a given time. To run the WRF model, three nested domain (D02, D03, and D04) have been considered inside a parent outer domain (D01). Configuration of domains and their resolution can be seen in Fig. 6.

These options have been considered in consultation with the Iran Meteorological Organization. The list of physics schemes used in this model can be seen in Table 1. In the domains 03 and 04, the cumulus parameterization has been turned off. In the larger domains, the Kain–Fritsch cumulus parameterization has been used.[33]

## 4.3 *InSAR Processing*

Repeat orbit interferometry package and Delft object-oriented radar interferometric software have been used to process the raw data and to produce interferograms. After the production of Single Look Complex data, the co-registration polynomial has been determined to resample slave data to the master grid. At this step, a single coarse offset between master and slave data

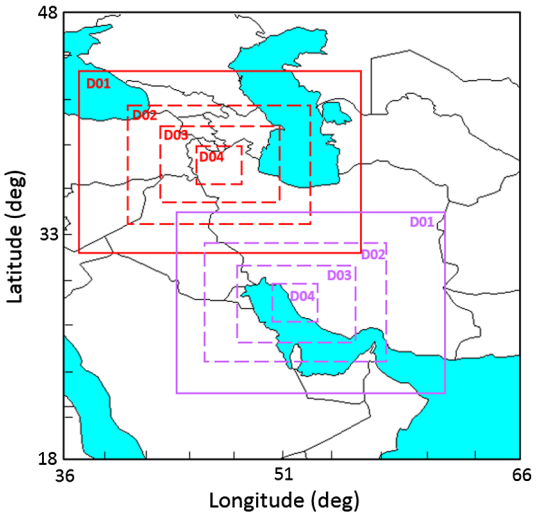


**Fig. 6** Configuration of domains around the study areas. The spatial resolution of the D01, D02, D03, and D04 is 27, 9, 3, and 1 km from the outside to the inside.

**Table 1** The physics schemes used in the WRF configuration.

| Category | Scheme | Reference |
|---|---|---|
| Longwave radiation | WRF single-moment 6 class | Ref. 28 |
| Shortwave radiation | Rapid radiative transfer model | Ref. 29 |
| Land surface | Goddard | Ref. 30 |
| Planetary boundary layer | Noah-MP (multiphysics) | Ref. 31 |
| Microphysics | Yonsei University | Ref. 32 |

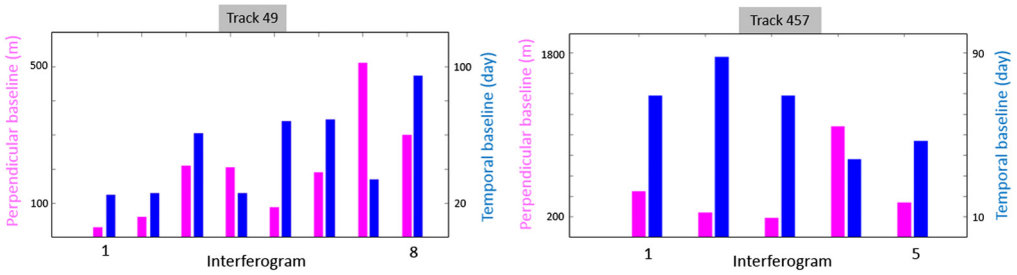


**Fig. 7** Perpendicular and temporal baselines of the interferograms.

have been estimated. Then the offset between master and slave data has been computed at a small patches. Finally, the co-registration has been done using the estimated polynomial. After this step, the coherence image and the interferogram have been produced using a multilook factor of 5 in azimuth and 1 in range. In the last step, phase unwrapping has been done to reconstruct the original phase from wrapped phase using Statistical-Cost, Network-Flow Algorithm for Phase Unwrapping software.[34]

To study the effect of different methods of tropospheric correction, several interferograms whose temporal baseline does not exceed 100 days in desired areas in Iran have been selected. According to geodynamic studies and reports, during this period, deformation of the areas can be neglected. Temporal and perpendicular baselines of considered interferograms are visible in Fig. 7.

## 4.4 *Results and Discussion*

In this section, the obtained results are examined. Figure 8 shows the example of unwrapped interferograms and differential tropospheric delay maps obtained from different correction methods in Bushehr area.

The tropospheric delay by integration method was computed in different cases, which could be abbreviated as follows.

- Using ERA-I and incidence angles (ERAIA) of each pixel.
- Using ERA-I and mean incidence angle (ERAMA).
- Using WRF outputs and incidence angles (WRFIA) of each pixel.
- Using WRF outputs and mean incidence angle (WRFMA).

Different types of ray tracing methods, including Thayer, PWL, RPWL, and 3D were also used to compute tropospheric delay.

The temporal baselines of interferograms are short and there are no reports of earthquakes during this period. For this reason, it can be said that there is no deformation signal in the unwrapped interferograms. On the other hand, due to correction of orbital and topography effects, it can be said that the unwrapped interferograms only include tropospheric effects and

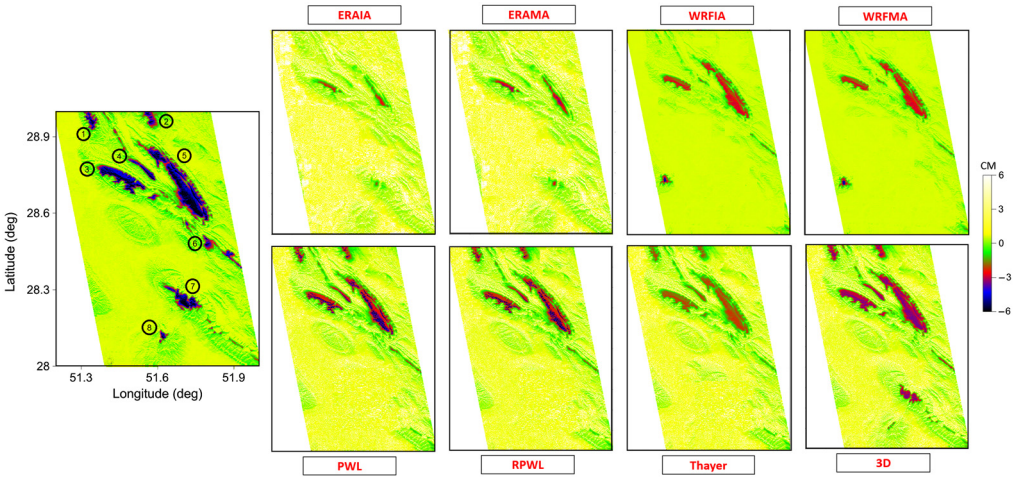


**Fig. 8** The example of unwrapped interferogram and the modeled tropospheric effect in Bushehr area using ERAIA, ERAMA, WRFIA, WRFMA, Thayer, PWL, RPWL, and 3D methods. The temporal baseline is 35 days.

residual noises. Therefore, it is expected that the differential tropospheric delay maps will have a significant compatibility to the unwrapped interferograms. Figure 8 shows a complex differential tropospheric delay maps. In Fig. 8, the eight sub-areas in the unwrapped interferograms are identified. The results show that some methods have not been able to detect the variations of these sub-areas. The main challenge is that which correction method could detect the location and size of the variations of the sub-areas. The maps obtained from ERAIA and ERAMA methods are very similar. This is also true for the WRFIA and WRFMA methods. This comparison shows that the use of an incidence angle for each pixel has no significant advantage compared with the use of the mean incidence angle in estimating the differential tropospheric delay. In general, integration methods were not successful in calculating the exact amount the sub-areas variations as much as ray tracing methods. The results obtained from the PWL and RPWL methods are also consistent. Clearly, ray tracing methods have more ability to detect the sub-areas variations. It seems that the 3D ray tracing method is more successful than other methods. The statistical result of unwrapped interferogram and differential tropospheric delay from different methods comparison are listed in Table 2. The least root-mean-square error (RMSE) is related to the 3D ray tracing method, and the maximum RMSE is related to the ERA-I method. Generally, the WRF model has more capability than the ERA-I model, but it should be noted that the WRF model has produced a completely wrong clear variations on the left side of the map. Ray tracing methods have been shown to be more capable of detecting sub-areas variations compared to integration methods. Regarding the comparison, it is clear that the 3D ray tracing method has the most accuracy in estimating the tropospheric signals in this case study. As mentioned above, in the 3D ray tracing method, unlike other ray tracing methods, a ray is free to move in 3D space. Therefore, it can be said that this feature has been effective in the results. For example, variations of sub-area 7 have been reproduced only by 3D ray tracing method. Based on previous studies, lateral variations of the troposphere in many cases can be neglected. Comparing the results of ray tracing techniques with other methods shows that these variations can be important and effective in some cases. Variations of sub-areas 6 and 8 are not detected by any of the correction methods. This can be due to inaccuracy of meteorological data.

After statistically comparing the results, it is necessary to check the impact of tropospheric correction methods in the spectral domain.[35] Figure 9 shows the variance spectra for each of the correction methods. In this paper, the discrete cosine transform have been used.[36] This transform avoids some of the problems with periodicity and trends, unlike the Fourier transform.[35,36] According to Fig. 9, it can be concluded that the ray tracing techniques reduce spectral power. This reduction is more clear for wavelengths longer than 30 km. Due to the large similarity of the results obtained from the two types of incidence angle, the results of the mean incidence angle

**Table 2** The statistical result of differential tropospheric delay from different methods compared to unwrapped interferogram in Bushehr area.

| Sub-area number | Successful methods and RMSE (cm) | | | | | | | |
|---|---|---|---|---|---|---|---|---|
| 1 | PWL | RPWL | Thayer | 3D | | | — | |
| | 3.5 | 3.1 | 3.2 | 2.5 | | | — | |
| 2 | PWL | RPWL | Thayer | 3D | | | — | |
| | 5.1 | 5.4 | 6.3 | 4.1 | | | — | |
| 3 | ERAIA | ERAMA | WRFIA | WRFMA | PWL | RPWL | Thayer 3D | — |
| | 7.8 | 7.1 | 6.1 | 5.7 | 4.2 | 4.7 | 5.2 | 3.7 |
| 4 | WRFIA | WRFMA | PWL | RPWL | Thayer | 3D | — | |
| | 6.7 | 6.4 | 4.4 | 4.7 | 5.3 | 3.9 | — | |
| 5 | ERAIA | ERAMA | WRFIA | WRFMA | PWL | RPWL | Thayer | 3D |
| | 7.8 | 7.6 | 5.9 | 5.3 | 3.9 | 3.7 | 4.6 | 2.9 |
| 6 | None of the methods have been successful | | | | | | | |
| 7 | 3D | | | | — | | | |
| | 7.5 | | | | — | | | |
| 8 | None of the methods have been successful | | | | | | | |

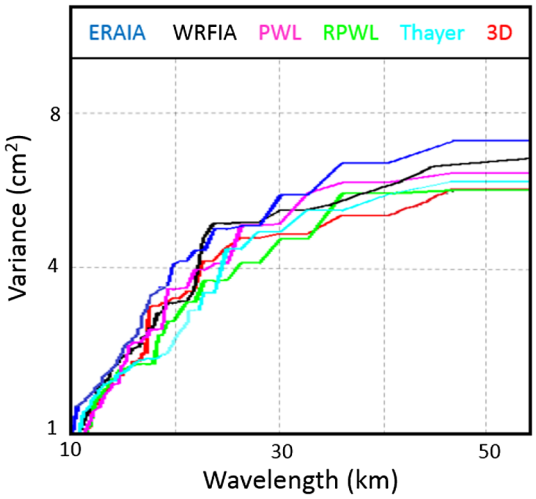


**Fig. 9** Spectra of variances for all correction methods.

have not been plotted. According to the above mentioned, eight interferograms have been produced over this area. The average RMSE between differential tropospheric delay from different methods and unwrapped interferograms can be seen in Fig. 10. Figure 10 shows that ray tracing techniques have more ability to model tropospheric variations between two acquisitions times.

Figure 11 shows the example of unwrapped interferograms and differential tropospheric delay maps obtained from different correction methods in Tabriz area. The unwrapped interferograms and differential tropospheric delay maps in Tabriz area show that the results of ray tracing technique have been more successful. It should be noted that the result of using an incidence angle is not different significantly from the result of using the incidence angle of each pixel in

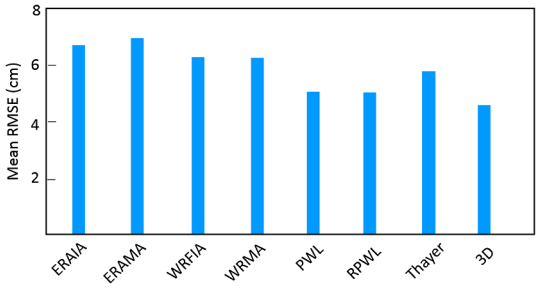


**Fig. 10** The average RMSE in Bushehr area.

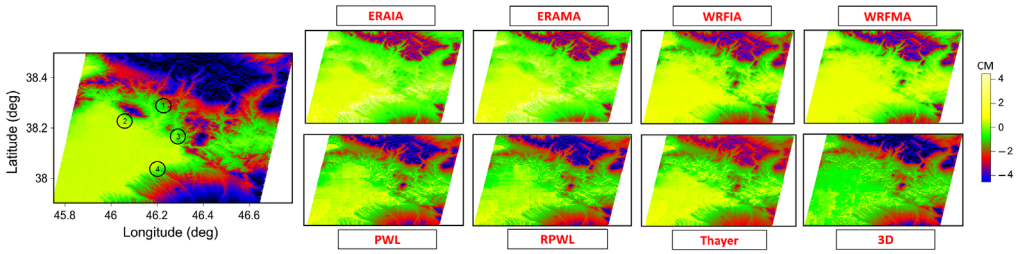


**Fig. 11** The example of unwrapped interferogram and the modeled tropospheric effect in Tabriz area using ERAIA, ERAMA, WRFIA, WRFMA, Thayer, PWL, RPWL, and 3D methods. The temporal baseline is 35 days.

**Table 3** The statistical result of differential tropospheric delay from different methods compared to unwrapped interferogram in Tabriz area.

| Sub-area number | Successful methods and RMSE (cm) | | | | | | | |
|---|---|---|---|---|---|---|---|---|
| 1 | ERAIA | ERAMA | WRFIA | WRFMA | PWL | RPWL | Thayer | 3D |
| | 3.9 | 3.4 | 3 | 2.8 | 2.3 | 2.4 | 2.8 | 1.8 |
| 2 | None of the methods have been successful | | | | | | | |
| 3 | PWL | RPWL | Thayer | 3D | — | | | |
| | 3.2 | 2.9 | 3.7 | 2.8 | — | | | |
| 4 | ERAIA | ERAMA | WRFIA | WRFMA | PWL | RPWL | Thayer | 3D |
| | 3.8 | 3.6 | 3.5 | 3.4 | 2.5 | 2.4 | 3 | 1.6 |

Tabriz area also. In addition, the results obtained from the WRF model and the ERA-I model are very similar to each other.

Table 3 includes the statistical result of unwrapped interferogram and differential tropospheric delay from different methods comparison in Tabriz area. Variations of sub-area 2 is not detected by any of the correction methods. Similar to the previous interferogram, this can be due to inaccuracy of meteorological data. These comparisons show a significant difference between the results obtained from the ray tracing technique and the results obtained from integration methods.

Figure 12 shows the variance spectra of this cases study. It can be clearly stated that at wavelengths longer than 20 km the spectral power reduce in the results of ray tracing techniques. The average RMSE between differential tropospheric delay from different methods and five unwrapped interferograms can be seen in Fig. 13. Figure 13 shows that ray tracing techniques, especially the PWL, RPWL, and 3D methods, are more successful in calculating tropospheric variations.

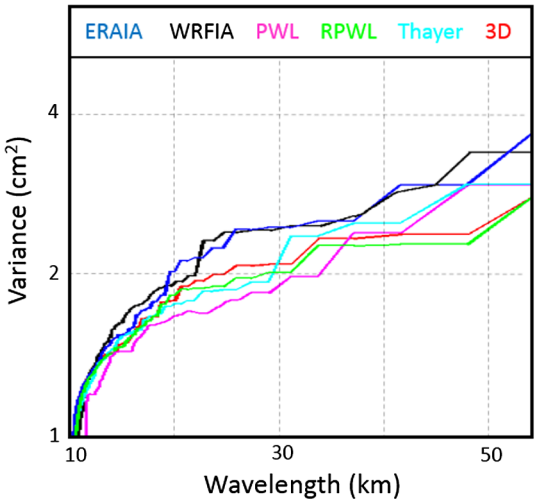


**Fig. 12** Spectra of variances for all correction methods.

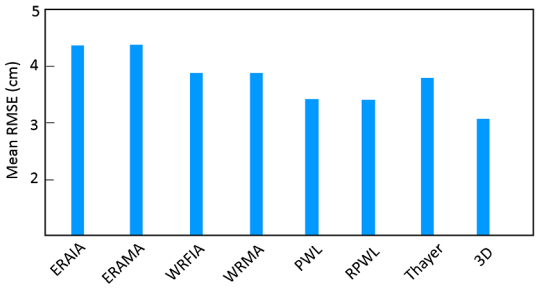


**Fig. 13** The average RMSE in Tabriz area.

## 5 Conclusion

This paper discussed and showed the efficiency of integration method and ray tracing techniques to correct the tropospheric effect on unwrapped interferogram. For this purpose, a number of ASAR/ENVISAT acquisitions, ERA-I data, and WRF model outputs were used. Four different integration methods of tropospheric correction were compared and discussed with four methods of ray tracing technique in two areas. The results of the ERA-I data and WRF model were very similar in integration methods. Also, the use of an incidence angle for each pixel did not make much difference in the results. The most important result of this study was that the ray tracing techniques produce more precise differential tropospheric delay maps compare to the integration methods. The ray tracing techniques were more efficient than other methods, because these techniques takes into account the lateral variations of the tropospheric parameters, which is neglected in other methods.

## Acknowledgments

Authors would like to appreciate the European Space Agency and ECMWF for providing the radar acquisitions and ERA-I data, respectively.

## References

1. H. A. Zebker, P. A. Rosen, and S. Hensley, "Atmospheric effects in interferometric synthetic aperture radar surface deformation and topographic maps," *J. Geophys. Res.* **102**(B4), 7547–7563 (1997).

2. A. L. Gray, K. E. Mattar, and G. Sofko, "Influence of ionospheric electron density fluctuations on satellite radar interferometry," *Geophys. Res. Lett.* **27**, 1451–1454 (2000).
3. S. Haji-Aghajany, B. Voosoghi, and A. Yazdian, "Estimation of north Tabriz fault parameters using neural networks and 3D tropospherically corrected surface displacement field," *Geomatics Nat. Hazards Risk* **8**(2), 918–932 (2017).
4. D. Remy et al., "Accurate measurement of tropospheric effects in volcanic areas from SAR interferometry data: application to Sakurajima volcano (Japan)," *Earth. Planet. Sci. Lett.* **213**, 299–310 (2003).
5. O. Cavalié et al., "Ground motion measurement in the Lake Mead area, Nevada, by differential synthetic aperture radar interferometry time series analysis: probing the lithosphere rheological structure," *J. Geophys. Res.* **112**(B3), B03403 (2007).
6. J. R. Elliott et al., "InSAR slip rate determination on the AltynTagh Fault, northern Tibet, in the presence of topographically correlated atmospheric delays," *Geophys. Res. Lett.* **35**, L12309 (2008).
7. G. Peltzer et al., "Transient strain accumulation and fault interaction in the Eastern California shear zone," *Geology* **29**(11), 975–978 (2001).
8. D. A. Schmidt et al., "Distribution of aseismic slip rate on the Hayward fault inferred from seismic and geodetic data," *J. Geophys. Res.* **110**, B08406 (2005).
9. T. R. Emardson, M. Simons, and F. H. Webb, "Neutral atmospheric delay in interferometric synthetic aperture radar applications: statistical description and mitigation," *J. Geophys. Res.* **108**(B5), 2231 (2003).
10. R. Jolivet et al., "Improving InSAR geodesy using global atmospheric models," *J. Geophys. Res. Solid Earth* **119**, 2324–2341 (2014).
11. S. Haji-Aghajany and Y. Amerian, "Atmospheric phase screen estimation for land subsidence evaluation by InSAR time series analysis in Kurdistan, Iran," *J. Atmos. Solar-Terrestrial Phys.* **164**, 81–88 (2020).
12. J. Bohm and H. Schuh, "Vienna maping function in VLBI analysis," *J. Geophys. Res Lett.* **31**(1), L01603 (2004).
13. S. Haji-Aghajany et al., "An optimal troposphere tomography technique using the WRF model outputs and topography of the area," *Remote Sens.* **12**(9), 1442 (2020).
14. S. Haji-Aghajany, Y. Amerian, and S. Verhagen, "B-spline function-based approach for GPS tropospheric tomography," *GPS Solutions* **24**, 88 (2020).
15. A. Hofmeister, Determination of Path Delays in the Atmsophere for Geodetic VLBI bu Means of Ray Tracing, Vienna University of Technology (2016).
16. S. Haji-Aghajany and Y. Amerian, "Three dimensional ray tracing technique for tropospheric water vapor tomography using GPS measurements," *J. Atmos. Solar-Terr. Phys.* **164**, 81–88 (2017).
17. S. Haji-Aghajany, B. Voosoghi, and Y. Amerian, "Estimating the slip rate on the north Tabriz fault (Iran) from InSAR measurements with tropospheric correction using 3D ray tracing technique," *Adv. Space Res.* **64**(11), 2199–2208 (2019).
18. G. Huadong et al., "Yushu earthquake synergic analysis study using multi-modal SAR datasets," *Chin. Sci. Bull.* **55**(31), 3499–3503 (2010).
19. A. Ferretti, C. Prati, and F. Rocca, "Permanent scatters in SAR interferometry," *IEEE Trans. Geosci. Remote Sens.* **39**(1), 8–20 (2001).
20. P. Berardino et al., "A new algorithm for surface deformation monitoring based on small baseline differential SAR interferometry," *IEEE Trans. Geosci. Remote Sens.* **40**(11), 2375–2383 (2002).
21. D. P. Dee et al., "The ERA-Interim reanalysis: configuration and performance of the data assimilation system," *Q. J. R. Meteorol. Soc.* **137**(656), 553–597 (2011).
22. M. Rahimzadegan and M. R. Mobasheri, "An attempt for improving MODIS atmospheric temperature profiles products in clear sky," *Meteorol. Appl.* **18** (2), 181 (2011).
23. M. Merrikhpour and M. Rahimzadegan, "Analysis of temporal and spatial variations of total precipitable water vapor in western Iran using radiosonde and MODIS measurements," *J. Appl. Remote Sens.* **13**(4), 044508 (2019).
24. M. Gamshadzaei and M. Rahimzadegan, "Particle swarm optimization based water index (PSOWI) for mapping the water extents from satellite images," *Geocarto Int.* (2019).

25. S. Haji-Aghajany and Y. Amerian, "Hybrid regularized GPS tropospheric sensing using 3-D ray tracing technique," *IEEE Geosci. Remote Sens. Lett.* **15**, 1475–1479 (2018).
26. J. Michalakes et al., "The weather reseach and forecast model: software architecture and performance," in *Proc. 11th ECMWF Workshop on the Use of High Perform. Comput. Meteorol.*, G. Mozdzynski Ed., Reading (2004).
27. W. C. Skamarock et al., *A Description of the Advanced Research WRF, Version 3*, pp. 1–113, National Center For Atmospheric Research Boulder Co Mesoscale and Microscale Meteorology Division, Boulder, Colorado (2008).
28. S.-Y. Hong and J.-O. J. Lim, "The WRF single-moment 6-class microphysics scheme (WSM6)," *J. Korean Meteorol. Soc.* **42**, 129–151 (2006).
29. M. J. Iacono et al., "Radiative forcing by long-lived greenhouse gases: Calculations with the AER radiative transfer models," *J. Geophys. Res.* **113**, D13103 (2008).
30. M.-D. Chou and M. J. Suarez, *A Solar Radiation Parameterization For Atmospheric Studies*, Technical Report Series on Global Modeling and Data Assimilation, Vol. 15, NASA/TM-1999-104606, NASA, Washington, DC (1999).
31. G.-Y. Niu et al., "The community Noah land surface model with multiparameterization options (Noah-MP): 1. Model description and evaluation with local-scale measurements," *J. Geophys. Res. Atmos.* **116**, D12 (2011).
32. S. Y. Hong, Y. Noh, and J. Dudhia, "A new vertical diffusion package with an explicit treatment of entrainment processes," *Mon. Weather Rev.* **134**, 2318–2341 (2006).
33. J. S. Kain, "The Kain–Fritsch convective parameterization: an update," *J. Appl. Meteorol.* **43**, 170–181 (2004).
34. SNAPHU, "Statistical-cost, network-flow algorithm for phase unwrapping (SNAPHU)," Stanford University, 2005, http://www-star.stanford.edu/sar
35. J. Foster et al., "Mitigating atmospheric noise for InSAR using a high resolution weather model," *Geophys. Res. Lett.* **33**, L16304 (2006).
36. B. Denis, J. Côté, and R. Laprise, "Spectral decomposition of two-dimensional atmospheric fields on limited-area domains using the discrete cosine transform (DCT)," *Mon. Weather Rev.* **130**, 1812–1829 (2002).

**Saeid Haji-Aghajany** is currently a PhD candidate under the supervision of Dr. Yazdan Amerian at K. N. Toosi University of Technology, Tehran, Iran. He is also a researcher at Delft University of Technology. His main research interests include global navigation satellite systems (GNSS) meteorology, GNSS remote sensing, and deformation monitoring using GPS and InSAR observations.

**Yazdan Amerian** received his BSc degree in geomatics engineering from the University of Tehran and his MSc and PhD degrees in geodesy from K. N. Toosi University of Technology, Tehran, Iran. He is now an assistant professor with Faculty of Geodesy and Geomatics Engineering, K. N. Toosi University of Technology. His main research interests include satellite geodesy, GNSS, and GNSS remote sensing.